INTERNATIONAL JOURNAL FOR NUMERICAL METHODS IN FLUIDS
Int. J. Numer. Meth. Fluids 2009; **59**:117–146
Published online 2 June 2008 in Wiley InterScience (www.interscience.wiley.com). DOI: 10.1002/fld.1802

The combined effects of non-planarity and asymmetry on primary and secondary flows in the small bronchial tubes

B. Soni[1], C. Lindley[1] and D. Thompson[2,*,†]

[1]*Computational Simulation and Design Center, Mississippi State University, Mississippi State, MS 39762, U.S.A.*
[2]*Department of Aerospace Engineering, Mississippi State University, Mississippi State, MS 39762, U.S.A.*

SUMMARY

The laminar flow in the small bronchial tubes is quite complex due to the presence of vortex-dominated, secondary flows. In this paper, we report the results of a numerical investigation of the simultaneous effects of asymmetric and non-planar branching on the primary and secondary flows in the small bronchial tubes, i.e. generations 6–12. We simulate steady-state inspiratory flow at a Reynolds number of 1000 in three-generation, asymmetric planar and non-planar bronchial tube models. The non-planar model was defined by applying a 90° out-of-plane rotation to the third-generation branches. A detailed mesh refinement study was performed in order to demonstrate mesh independence. Significant differences were observed between flows in the planar and non-planar models. An uneven mass flow distribution was observed in the non-planar model in contrast to the evenly distributed mass flow in the planar model. The secondary flows created symmetric vortex patterns in the planar model, whereas vortex symmetry was lost in the non-planar model. These results illustrate the importance of incorporating asymmetry in addition to non-planarity in the geometric models. Copyright © 2008 John Wiley & Sons, Ltd.

Received 8 July 2007; Revised 13 February 2008; Accepted 17 February 2008

KEY WORDS: bifurcation; non-planar; bronchial tube flow; asymmetric

1. INTRODUCTION

Respiration produces surprisingly complex flow fields in the network of lung airways. Secondary currents, in the form of vortices, play a critical but poorly understood role in the filtration of entrained particles from inhaled air, consigning some to deposition on mucus-lined walls, others to a return trip through exhalation, and some to lodgings deep in the fine structures of the terminal airways. The motivation for this effort is the significance of two seemingly dichotomous

*Correspondence to: D. Thompson, Department of Aerospace Engineering, P.O. Box A, Mississippi State University, Mississippi State, MS 39762, U.S.A.
†E-mail: dst@ae.msstate.edu

Contract/grant sponsor: National Science Foundation; contract/grant numbers: EPS-0556308, ITR/NGS-0326386

applications that are related to airflow in the lungs (1) the health hazard posed by the inhalation of carcinogenic, disease-bearing, or lung-damaging aerosols and (2) the clinical delivery of both local and systemic aerosolized drugs through the lungs. Progress on both applications is hampered by the fact that experimental studies for flow in the small bronchial tubes are difficult and expensive due to their small scale and their inaccessibility deep in the chest. In addition, there are ethical issues associated with such *in vivo* experimental studies.

1.1. Flows in bronchial tubes

The flows in the small bronchial tubes are characterized by a Reynolds number less than 1000 [1]. The general characteristics of the bronchial tube flow field are illustrated in Figures 1 and 2. The flow in the direction of the local axis of the tube is designated as the primary flow and the flow in the plane perpendicular to the axis of the tube as the secondary flow. It should be noted that these definitions for the primary and secondary flows are only valid for simple tubes. As it is not possible to define a local tube axis near the bifurcation, the primary and secondary flow designations have little meaning in this region. Figure 1 shows the primary velocity profiles at various cross-sections. The vectors are colored by normalized velocity magnitude. Figure 2(a) shows a plot of stream ribbons colored according to the exit in which the ribbon leaves the domain. This figure illustrates the effects of the secondary flows, which are dominated by vortices. The ribbons are twisted near the bifurcation indicating the presence of these vortices. The cross-flow velocity vectors, representing the secondary flow in cutting plane AB in Figure 1, are shown in Figure 2(b). The vectors are plotted on the cutting plane, which is colored by total velocity magnitude. Only every third vector is plotted for clarity. The vortices are formed due to the axial curvature of the tube. As a fluid particle enters the curved section of the tube, its path changes due to the curvature. To conserve angular momentum, the particle velocity increases. As particles on the inside of the curve, where the radius of curvature is smaller, experience a greater change in path curvature, they accelerate more than those on the outside of the curve. These faster particles

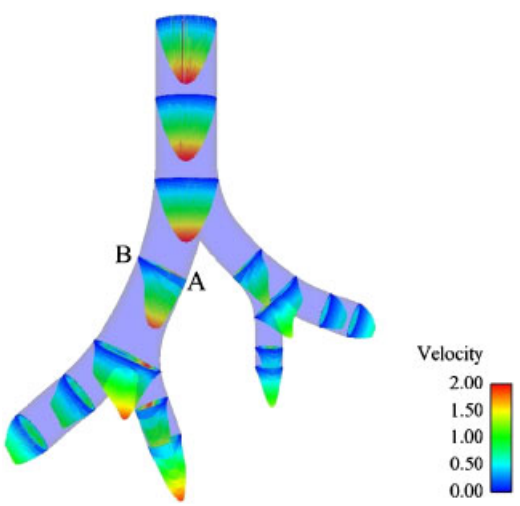

Figure 1. Primary flow in three-generation bronchial tube model—axial velocity profiles at various cross-sections colored by velocity magnitude.

DOI: 10.1002/fld

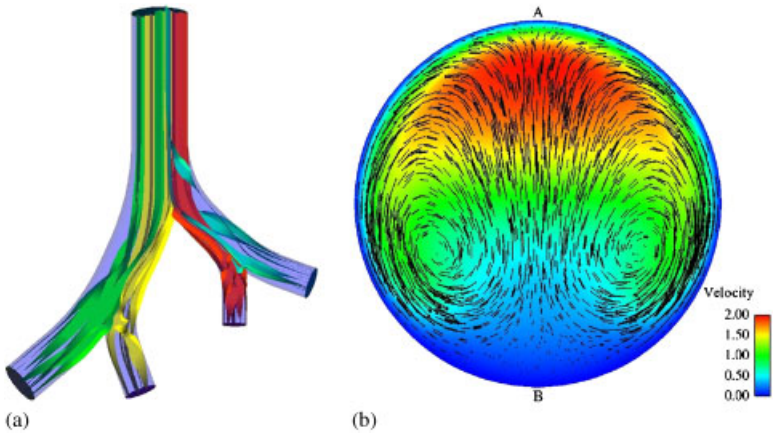

Figure 2. Secondary flows in three-generation bronchial tube model: (a) stream ribbons colored by exit and (b) counter-rotating vortex pair in cutting plane AB (plane shaded by velocity magnitude).

rush to the outside of the curve and displace the slower moving particles, which results in the formation of a counter-rotating vortex pair. This phenomenon is illustrated in Figure 2(b) where the region of highest velocity, i.e. the red shaded region, is shifted toward the outside of the turn (A side) due to inertial effects. Vortices generated due to axial curvature are typically called Dean vortices [2].

1.2. Literature review

There have been a number of experimental and computational studies investigating bronchial tree flow fields with and without particle transport. A variety of bronchial tube geometries such as symmetric and asymmetric, single- and multi-generation, planar and non-planar have been employed to study both steady and unsteady flows. The importance of mesh-independent numerical solutions has been recognized and demonstrated in some simulations of bronchial tube flows.

1.2.1. Lung geometry. Morphological descriptions of the human bronchial tubes have appeared in the literature since 1963 when Weibel [3] introduced a symmetric physical model. Horsfield and Cumming introduced an anatomical representation of asymmetric lung tubes taking Weibel's model as the fundamental unit [4]. Hammersley and Olson presented symmetric and asymmetric bifurcation patterns for the human lung appropriate for generations 6–12 [5]. In 2004, Hegedus *et al.* provided a detailed mathematical description of a morphologically realistic airway geometry of the first five generations [6].

1.2.2. Secondary flows and particle deposition. The influence of vortices in lung airway flows has been demonstrated to be significant. Schroter and Sudlow [7] experimentally studied the flow in two- and three-generation bronchial tube models for steady-state inspiratory and expiratory conditions over a Reynolds number range of 100–4500. The velocity profiles were observed to be skewed toward the outside of the turn in the plane of the bifurcation in the second-generation daughter tubes. In addition, 'M-shaped' velocity profiles were observed in the plane normal to the

DOI: 10.1002/fld

bifurcation due to the presence of secondary flows. When steady-state flow with particle deposition was simulated for micron-sized particles at a Reynolds number of 568 [8, 9], secondary flows were observed to play an important role in particle deposition for inspiratory conditions. Gatlin *et al.* [1] observed the magnitude of secondary velocities to be as high as 50% of the local axial velocity for flow at a Reynolds number of 500 in an asymmetric bifurcation. Stronger secondary currents were observed by Liu *et al.* [10] in an asymmetric model compared with a symmetric model in steady-state flow field simulations. The flow was simulated using an unstructured mesh and mesh convergence was demonstrated by refinement until changes in mass flow rate were within a tolerance of 0.5%. Soni and Thompson [11] investigated secondary flows in planar three- and four-generation asymmetric models. They used a uniform inlet flow profile and had difficulties obtaining mesh-independent solutions for the secondary flows.

Zhang *et al.* [12] simulated particle deposition for a four-generation symmetric model using a parabolic inlet velocity profile on a structured mesh refined to show mesh independence. They demonstrated the effects of inlet profiles on particle deposition patterns. Zhang *et al.* [13] compared microparticle and nanoparticle deposition patterns in a planar three-generation upper airway for different inspiratory conditions. The metrics used to measure mesh independence included the velocity fields, mass fractions, and particle deposition patterns. The nanoparticles were observed to be more uniformly distributed along the airway than were the microparticles. Balashazy *et al.* [14] simulated fiber deposition in a planar three-generation central airway. The particle deposition efficiency was examined for flow rates varying over the range of 10–120 l/min, which correspond to resting and heavy exercise, respectively, and fiber lengths ranging from 25 to 100 μm for different geometries with varying branching angles. The deposition efficiency increased with increasing breathing rates and branching angles, demonstrating the significance of flow rate and airway geometry on fiber deposition. Longest and Vinchurkar [15] compared four different mesh styles—multi-block-structured hexahedral, unstructured tetrahedral, solution adaptive tetrahedral, and hybrid mesh—to study bronchial tube flow fields and particle deposition. Comparisons were made based on the total number of volume elements, flow solver run time, and rate of mesh convergence. Based on these criteria, the block-structured hexahedral mesh was shown to provide the optimum results.

1.2.3. Effects of non-planarity. In reality, the lung airways are not confined to a single plane. In addition to non-planar branching, the individual bifurcations may not have a plane of symmetry [16]. This asymmetry is typically neglected in the experimental studies and simulations reported in the literature. We adopt the terminology employed in the literature and use 'non-planar' to refer to out-of-plane branching of subsequent generations.

In most cases, the effects of non-planarity were evaluated under the assumption that the most extreme effects occur when the out-of-plane branch is perpendicular to the previous branch. The effects of non-planarity on microparticle deposition were investigated in an experimental study of steady-state inhalation using a symmetric three-generation model with the Reynolds number varying between 283 and 4718 by Kim and Fisher [17]. Caro *et al.* [18] observed the impact of non-planarity to be significant in the vortex patterns in an experimental effort to understand steady inspiratory flows in a three-generation symmetric bronchial tube model. Comer *et al.* [19] simulated microparticle deposition patterns for different Reynolds numbers, Stokes numbers, inlet particle release patterns, and airway geometry in a symmetric three-generation lung airway model. The particle deposition results, described in terms of patterns and surface concentrations, were found to be considerably different for the non-planar case in comparison with the planar case.

DOI: 10.1002/fld

Liu *et al*. [20] observed an uneven flow distribution as more flow entered the medial tubes than the lateral tubes in a symmetric three-generation planar model. In contrast, evenly distributed flow was observed in a symmetric three-generation non-planar bronchial tube model. Zhang and Kleinstreuer [21] claimed that the microparticle deposition patterns for the non-planar model were equivalent to the planar model, but rotated. Additionally, the secondary flow intensity was found to be about 120% higher during exhalation in a non-planar model than in a planar model, where the intensity of the secondary flow was defined as the ratio of integrated secondary velocities to integrated axial velocities at a given cross-section. Particle deposition patterns were calculated for normal breathing and high-frequency ventilation conditions employing a structured mesh that was refined to produce a mesh-independent solution in terms of the velocity profile.

1.2.4. Flow simulation for the complete bronchial tree. Researchers ultimately want to understand the flow structures and particle transport process in the entire human bronchial network. It has been a challenge to achieve this goal due to the complexity associated with the geometry of the human lungs. However, a few researchers have successfully simulated the flow in models with numerous generations. Nowak *et al*. [22] presented flow field and particle transport simulation results for lung airways generated from a CT scan. Comparisons of computational results for a realistic model and Weibel's symmetric planar entire lung airway model showed microparticle deposition patterns that exhibited moderate differences over a Reynolds number range of 120–2000 for both steady and unsteady flows. Although a CT scan model provides a more realistic geometry, it cannot provide the airway beyond nine generations, which limits its application for studying the entire lung airway. Ertbruggen *et al*. [23] described a three-dimensional anatomically based lung airway model starting from the trachea to the segmental bronchi containing 17 bifurcations for simulating steady-state flows with microparticle transport. The maximum particle deposition was found when the out-of-plane angle was largest compared with other tubes in the same generation, elucidating the role of non-planarity on deposition of micron-sized particles. A multi-block-structured mesh was chosen and refined until the maximum difference between velocity profiles was less than 2%.

1.3. Motivation

After reviewing the literature, the following statements can be made:

1. Although the effects of non-planarity and asymmetry in the bronchial tube geometry have been investigated individually, the combined effects of non-planarity and asymmetry have not been investigated.
2. Only a limited number of mesh refinement studies for bronchial flow field simulations have appeared in the literature [10, 12, 15, 20, 21, 23]. The mesh refinement studies seem rather incomplete as secondary flows were not considered, even though secondary flows play a crucial role in particle deposition.

In this paper, we focus on the areas that were not addressed in previous studies, namely

1. We investigate the effects of simultaneous asymmetry and non-planarity on the primary and secondary flows in bronchial tube models.
2. We present the results of detailed mesh refinement studies designed to demonstrate mesh independence of the primary and secondary flow fields in the bronchial tube models.

DOI: 10.1002/fld

2. NUMERICAL SIMULATION

2.1. Geometrical model

The asymmetric bronchial tube model described by Hammersley and Olson [5], which is appropriate for generations 6–12, was employed in this effort. The geometry shown in Figure 3 is taken to be the fundamental unit of the network of airways in the lung. In the nomenclature employed here, the parent tube represents one generation and the two daughter tubes represent a second generation. In general, the number of exits for a network can be obtained from $N_{\text{exit}} = 2^{N-1}$, where N is the number of generations. The asymmetric branching is defined by a parent-to-daughter diameter ratio of $D/d = 1.143$ for the larger daughter tube and a ratio of $D/d = 1.515$ for the smaller daughter tube. The branch angles for the larger and smaller daughter tubes are 25° and 45°, respectively. The length to diameter ratio for all branches is $L/D = 3.0$. The length of a daughter tube is defined as the distance from the intersection of the tube centers at the starting bifurcation to the intersection of the tube centers at the ending bifurcation. According to Hammersley and Olson, the local radius of curvature of the carina is less than $0.1D$. In our model, we employed a radius of curvature of $0.005D$. The shape of the carina was preserved by employing a sufficient number of points on the defining curve when discretizing the carinal region.

In a realistic bronchial network, branching is not confined to a plane, i.e. the subsequent generations may not lie in the same plane. The out-of-plane branch angles are randomly distributed in a manner that allows the bronchial tube network to fill the available space without intersections. Following research reported in the literature [17–21], we introduce non-planarity by rotating the third generation 90° out-of-plane with respect to the second generation.

Based on the above geometrical information, three-generation planar and non-planar computational models were generated. The fundamental unit shown in Figure 3 can be used to develop multi-generation models by attaching it to a previous generation and maintaining the appropriate parent/daughter tube diameter ratios. To develop a three-generation bronchial tree, a fundamental unit is added at each exit of the two daughter tubes of a two-generation geometry. The fundamental unit is attached such that the daughter tube is positioned centrally on its parent tube

Figure 3. Fundamental unit of bronchial tree (two generations and a single bifurcation).

DOI: 10.1002/fld

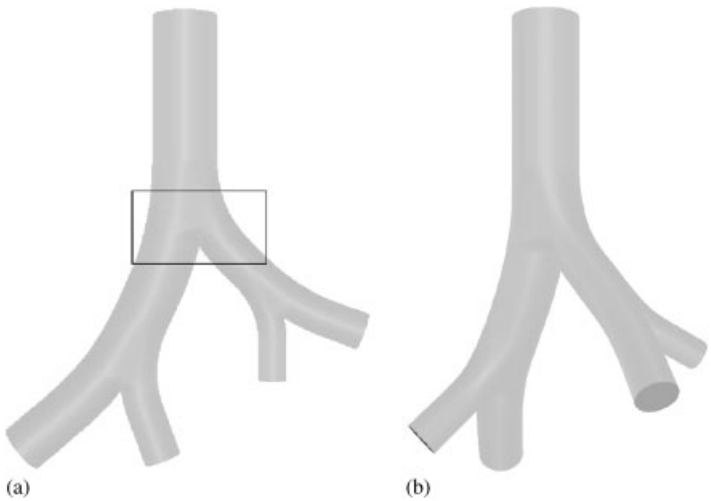

Figure 4. Three-generation bronchial tube geometries: (a) planar model showing location of the zoomed meshes in Figure 7 and (b) non-planar model rotated for better view.

to mimic the planar three-generation asymmetric model given by Hammersley and Olson [5]. In other words, in the planar model, the smaller tubes in the third generation were placed in the medial positions, whereas the larger tubes in the third generation were positioned laterally. Figures 4(a) and (b) show three-generation planar and non-planar geometries, respectively. The parent tube length was shortened in the fundamental unit to preserve the L/D ratio when attached to an exit of the previous generation.

2.2. Mesh generation

The computational domains for the bronchial tree models were discretized using unstructured meshes. In addition to advantages for modeling complex geometries relative to block-structured grids, the use of unstructured meshes facilitates improved load balancing for enhanced efficiency on large-scale parallel computers. However, an unstructured mesh may require more elements to reach the same level of accuracy as a structured mesh [15]. The unstructured mesh was generated using the SolidMesh package [24] that employs the advancing-front/local-reconnection technique developed by Marcum and Weatherill [25]. The advancing-front technique is used for the initial point placement. A combined Delaunay/min–max criterion is then used to reconnect the points to form volume elements. The code can create tetrahedral, pyramid, quadrilateral, prismatic, and hexahedral elements. The meshes generated for this study employed a surface mesh consisting of triangular elements and a mixed-element (hybrid) volume mesh.

One point should be made concerning the mesh generation strategy we used for the multi-generation models. If a uniform nodal distribution is employed for the surface mesh, each succeeding generation is less well resolved as the diameter of each tube decreases as the depth of the tree increases. This will likely result in an inadequately resolved flow field. We assume that, as each generation is geometrically similar to the fundamental unit, the primary flow structures in each generation are also geometrically similar. Although interference effects from preceding

DOI: 10.1002/fld

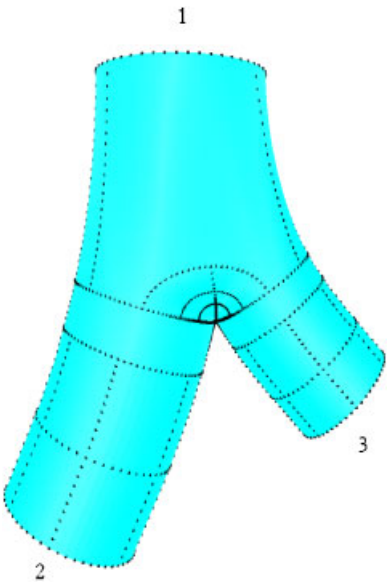

Figure 5. Self-similar nodal spacing for each tube. Cross-sections at 1, 2, and 3 have the same number of nodes distributed around their circumferences. In this image, the nodal spacing was doubled to enhance clarity.

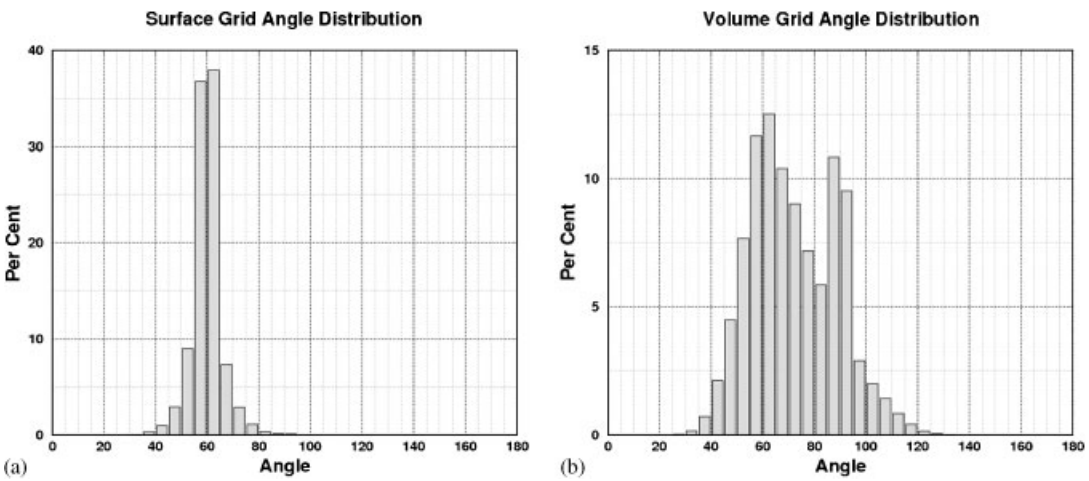

Figure 6. Mesh quality plots showing the distribution of included angles in the surface and volume meshes: (a) surface mesh quality and (b) volume mesh quality.

generations in the flow path render this statement false in a strict sense, it does provide some guidance for developing a systematic method for discretizing the computational domain. The assumption of geometrically similar flow structures implies that a geometrically similar surface mesh should be employed for each generation as the unstructured volume mesh is strongly

DOI: 10.1002/fld

dependent on the surface mesh. This was implemented by ensuring that the same number of nodes was employed to discretize geometrically similar parts in each generation. The geometry was subdivided as shown in Figure 5 to ensure a smooth transition from finer to coarser nodal spacing in the model. At cross-sections 1, 2, and 3, which are geometrically similar to one another, the same number of nodes were employed. In the coarsest mesh, 110 nodes were employed at each of these cross-sections. Although this does not guarantee that the mesh in a daughter tube is a geometrically similar copy of the mesh in its parent tube and, by inference, the mesh in its grandparent tube, it does ensure that a comparable mesh is employed in each generation. To preserve its shape, a finer nodal spacing was applied in the carinal region.

Mesh quality for an unstructured mesh is typically measured in terms of the included face angles. Standard mesh quality plots for the surface and volume meshes are shown in Figures 6(a) and (b). The average included angle for the surface triangles was 60° and more than 90% of the included angles were between 50° and 70° as shown in Figure 6(a). As seen in Figure 6(b), a majority of the included angles for the volume elements lie between 50° and 95°. As we employed a hybrid unstructured mesh, twin peaks occur in the volume mesh quality plot. The peak near 90° represents the quadrilateral faces on the prisms, whereas the peak near 60° represents the triangular faces in the prisms and tetrahedra. The average included angle for volume elements was 72°. Only 1.2% of the included angles were outside of a lower bound of 30° and an upper bound of 120°.

2.3. Mesh refinement strategy

To facilitate the mesh refinement study, four meshes were generated for the three-generation planar and non-planar models. The meshes for planar and non-planar models were generated using the same nodal spacing producing approximately the same number of elements for both geometries. Table I shows statistical information for each mesh generated for the planar and non-planar three-generation bronchial tube models. The number of elements was approximately doubled for each refinement by decreasing the nodal spacing in the surface mesh by a factor of $\sqrt[3]{2}$. Surface meshes near the initial bifurcation are shown for each mesh in Figure 7. Figures 7(a)–(d) show enlarged views of the surface mesh in the small rectangular region indicated in Figure 4(a).

It should be noted that the number of volume elements used in this mesh refinement study is relatively large in comparison with other mesh refinement studies reported in the literature [10, 12, 13, 15, 21, 23]. In addition to the obvious point that mesh convergence is strongly dependent

Table I. Statistical information for meshes generated for the three-generation planar and non-planar models.

Mesh	Nodes*	Surface elements*	Volume elements*
Baseline	1.29	0.29	5.5
Refinement 1	2.36	0.47	10.6
Refinement 2	4.29	0.74	20.15
Refinement 3	8.04	1.18	39.2

*The numbers are shown in millions.

DOI: 10.1002/fld

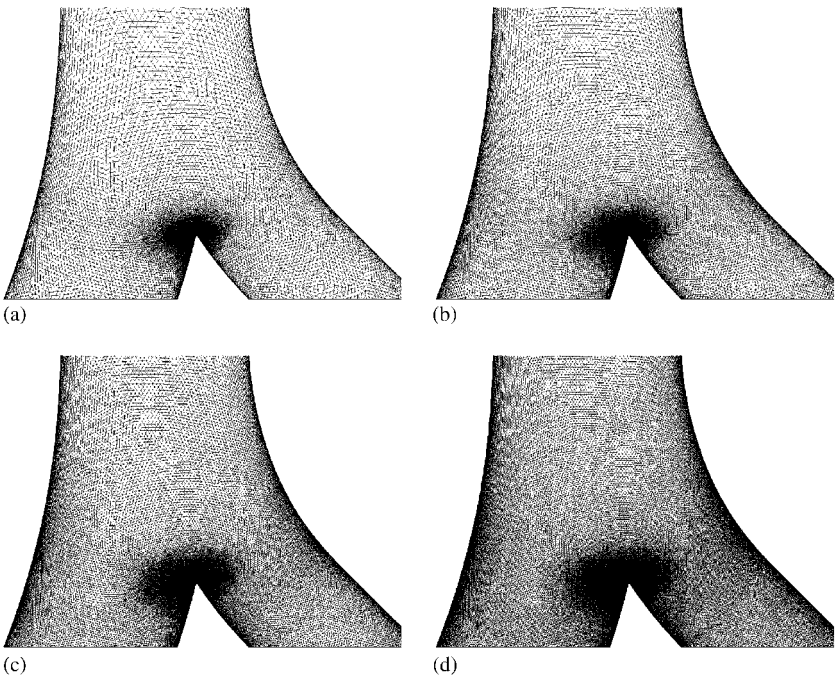

Figure 7. Detailed images showing the effects of surface mesh refinement near the first bifurcation as shown in Figure 4(a): (a) baseline mesh; (b) refinement 1; (c) refinement 2; and (d) refinement 3.

on the specific flow solver, we attribute this difference to the following. First, we have attempted to demonstrate mesh convergence using secondary flow field metrics, such as the vortex core location, which have not been employed in the past. Additionally, because of the relatively small radius of the carina, a larger number of nodes are needed to resolve the geometry in this region. Finally, an unstructured mesh requires more cells to provide the same level of accuracy as a structured mesh [15].

2.4. Flow solver

The steady flow solutions were computed using the unstructured unsteady computation of field equations (U^2NCLE) flow solver [26]. U^2NCLE is an unstructured, unsteady Reynolds-averaged Navier–Stokes code. The code uses a finite volume formulation of the Navier–Stokes equations, which satisfies a discrete approximation to the integral form of the conservation laws. Under the flow conditions in the small bronchial tubes, the fluid can be characterized by a constant density and viscosity. The flow is governed by the incompressible Navier–Stokes equations, which are based on the concepts of conservation of mass and momentum and are given in non-dimensional form in three dimensions as

$$\frac{\partial}{\partial \mathbf{t}} \int_{\Omega} Q \, \mathrm{d}V + \int_{\partial\Omega} \mathbf{F} \cdot \hat{n} \, \mathrm{d}A = \frac{1}{Re} \int_{\partial\Omega} \mathbf{G} \cdot \hat{n} \, \mathrm{d}A \tag{1}$$

DOI: 10.1002/fld

where

$$\mathbf{Q}=\begin{pmatrix} P \\ u \\ v \\ w \end{pmatrix} \tag{2}$$

$$\mathbf{F}=\begin{pmatrix} \beta u \\ u^2+P \\ uv \\ uw \end{pmatrix}\hat{i}+\begin{pmatrix} \beta v \\ uv \\ v^2+P \\ vw \end{pmatrix}\hat{j}+\begin{pmatrix} \beta w \\ uw \\ vw \\ w^2+P \end{pmatrix}\hat{k} \tag{3}$$

$$\mathbf{G}=\begin{pmatrix} 0 \\ \tau_{xx} \\ \tau_{yx} \\ \tau_{zx} \end{pmatrix}\hat{i}+\begin{pmatrix} 0 \\ \tau_{xy} \\ \tau_{yy} \\ \tau_{zy} \end{pmatrix}\hat{j}+\begin{pmatrix} 0 \\ \tau_{xz} \\ \tau_{yz} \\ \tau_{zz} \end{pmatrix}\hat{k} \tag{4}$$

where the viscous stresses are given as

$$\begin{aligned} \tau_{xx} &= 2\frac{\partial u}{\partial x} \\ \tau_{yy} &= 2\frac{\partial v}{\partial y} \\ \tau_{zz} &= 2\frac{\partial w}{\partial z} \\ \tau_{xy} &= \tau_{yx} = \frac{\partial u}{\partial y}+\frac{\partial v}{\partial x} \\ \tau_{xz} &= \tau_{zx} = \frac{\partial u}{\partial z}+\frac{\partial w}{\partial x} \\ \tau_{yz} &= \tau_{zy} = \frac{\partial v}{\partial z}+\frac{\partial w}{\partial y} \end{aligned} \tag{5}$$

Here u, v, and w are the fluid velocities in the x, y, and z directions, respectively, and P is the pressure. The above equations are non-dimensionalized by the reference density ρ_{ref}, the reference velocity U_{ref}, the reference viscosity μ_{ref}, and the characteristic length scale L, in this case, the diameter of the parent tube. The non-dimensional pressure is given as $P=(P^*-P_{\text{ref}})/(\rho_{\text{ref}}U^2{}_{\text{ref}})$, where P^* is the local static pressure. The Reynolds number is defined as $Re=\rho_{\text{ref}}U_{\text{ref}}L/\mu_{\text{ref}}$. As all variables are non-dimensionalized, the density and the viscosity do not appear explicitly in the equations. Finally, $\hat{n}$ is an outward-pointing unit vector for a given cell face. To solve the incompressible Navier–Stokes equations, an artificial compressibility term is added to the equations [27]. β is the artificial compressibility factor. Residual norms were reduced to 10^{-17}

DOI: 10.1002/fld

using local time stepping to converge to a steady-state solution. Typically, about 12 000 time steps were required to reach a steady state. All computations were made using 64 processors in parallel on a cluster consisting of 512 Sun Microsystems SunFire X2200 M2 servers.

2.4.1. Boundary conditions. The no-slip boundary condition was applied at the tube surface along with a zero normal pressure gradient assumption. The walls were assumed to be rigid and smooth. The velocity distribution at the inlet was specified explicitly. This defines the flow rate and differs from imposing a pressure difference between the inlet and outlet, which requires adjusting the pressure difference to achieve the desired flow rate. It also gives flexibility to introduce different inlet velocity profiles. In this study, the fully developed parabolic inlet velocity profile was employed. The parabolic inlet velocity profile is given by

$$V(r) = V_{\max}\left(1 - \left(\frac{r}{R}\right)^2\right) \tag{6}$$

where $V(r)$ is the inlet velocity, the non-dimensionalized maximum velocity is $V_{\max} = 2$, r is the radial position in the inlet plane, and R is the radius of the tube at the inlet. A constant static pressure was specified at each of the four outlets, assuming the same pressure at each of the third-generation outlets. The pressure at the inlet was allowed to float in response to the imposed values of exit pressure.

The assumption that the pressure at each exit is the same is not realistic considering the fact that the bronchial tubes are not equally ventilated. Owing to the lack of precise knowledge of the pressure at the corresponding locations in the actual bronchial tree, like many other researchers, we have imposed the same pressure at each exit [1, 12, 13, 19, 22, 23]. Obviously, this will have some impact on the results, in particular, flow partitioning. However, the primary intent of this paper is to investigate geometric effects on the flow. Evaluating the sensitivity to exit boundary conditions is a topic for continued research.

3. RESULTS

In this section, we present results from simulations of flow fields in planar and non-planar asymmetric three-generation airway models. These flows were simulated using the four meshes described in Table I. The simulations were performed for a Reynolds number of 1000 based on the initial parent tube diameter and mean velocity. We investigate the combined effects of the non-planarity and asymmetry on the primary and secondary flows. We also demonstrate mesh convergence of the primary and secondary flows for each configuration. To determine the locations and orientations of the curves and surfaces from which data were extracted, see Figure 8. In the descriptions that follow, we will refer to the bifurcation plane and the normal to the bifurcation plane. Figure 9 shows three-dimensional surface plots of axial velocity profiles at aa'. Figure 9(a) shows the orientation of the bifurcation plane, which is the plane of symmetry of the local bifurcation, and the intersection of the axial velocity profile with the bifurcation plane. Figure 9(b) shows the plane normal to the bifurcation plane and the intersection of the axial velocity profile with this plane.

DOI: 10.1002/fld

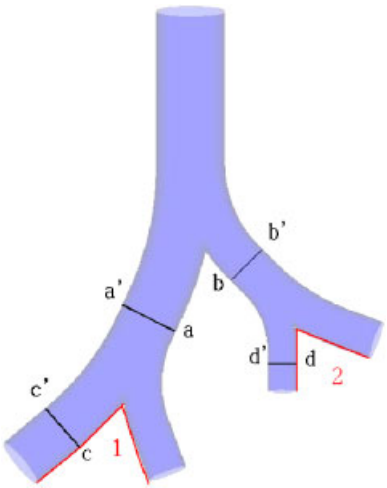

Figure 8. Locations of curve segments 1 and 2 as well as cutting planes aa', bb', cc' and dd'.

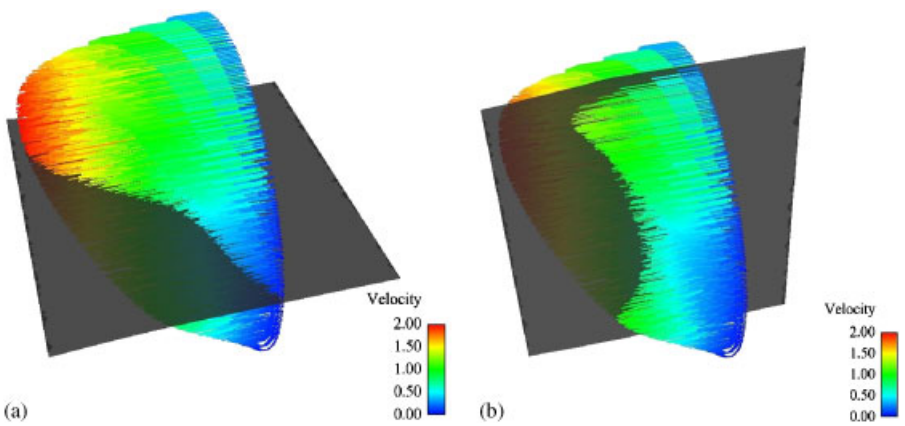

Figure 9. Three-dimensional surface plots of axial velocity profiles at aa' showing orientation of bifurcation plane and the plane normal to the bifurcation plane. Intersection of velocity profile with (a) bifurcation plane and (b) plane normal to bifurcation plane.

3.1. Mesh convergence of the primary flow

The mesh refinement study for the primary flow is accomplished employing the changes in the skin friction coefficient, mass flow distribution, and axial velocity profiles between meshes as metrics.

3.1.1. Skin friction coefficient near bifurcation. The sensitivity of the solution to the mesh can be demonstrated by observing changes in the skin friction coefficient as the mesh is refined. The

DOI: 10.1002/fld

non-dimensional skin friction coefficient c_f can be defined in terms of the wall shear stress τ_w as

$$c_f = \frac{2\tau_w}{\rho_{ref} U_{ref}^2} \tag{7}$$

As c_f is dependent on wall shear stress (which is a function of velocity derivatives), it is quite sensitive to mesh spacing. Skin friction data were extracted along the intersection of a plane with the tube surface in the carinal regions of each of the second-generation bifurcations to ascertain if the solution is independent of the mesh in these regions. These curves are indicated by the thickened lines and the numbers 1 and 2 in Figure 8. The skin friction coefficient plots for the planar and non-planar models are shown in Figures 10 and 11, respectively. In Figures 10(a), (c) and 11(a), (c), the differences in c_f between the refinements are not visible. Detailed views of selected intervals are shown in Figures 10(b), (d) and 11(b), (d) for better clarity. The detailed plots show that the differences decrease as the mesh is refined. This suggests that the solution is approaching mesh independence. It should be noted that there are still small differences between

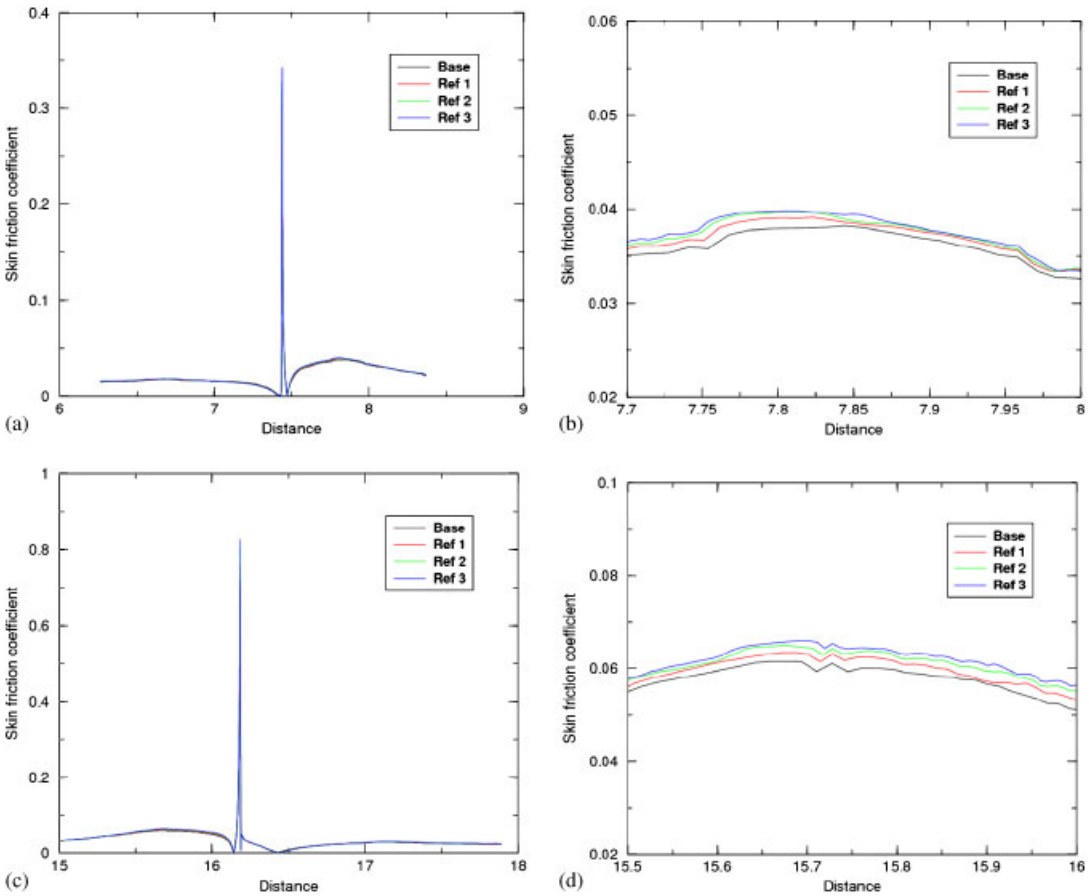

Figure 10. Distribution of skin friction coefficient c_f for the planar three-generation bronchial tube model: (a) segment 1 (b) segment 1 (detail); (c) segment 2; and (d) segment 2 (detail).

DOI: 10.1002/fld

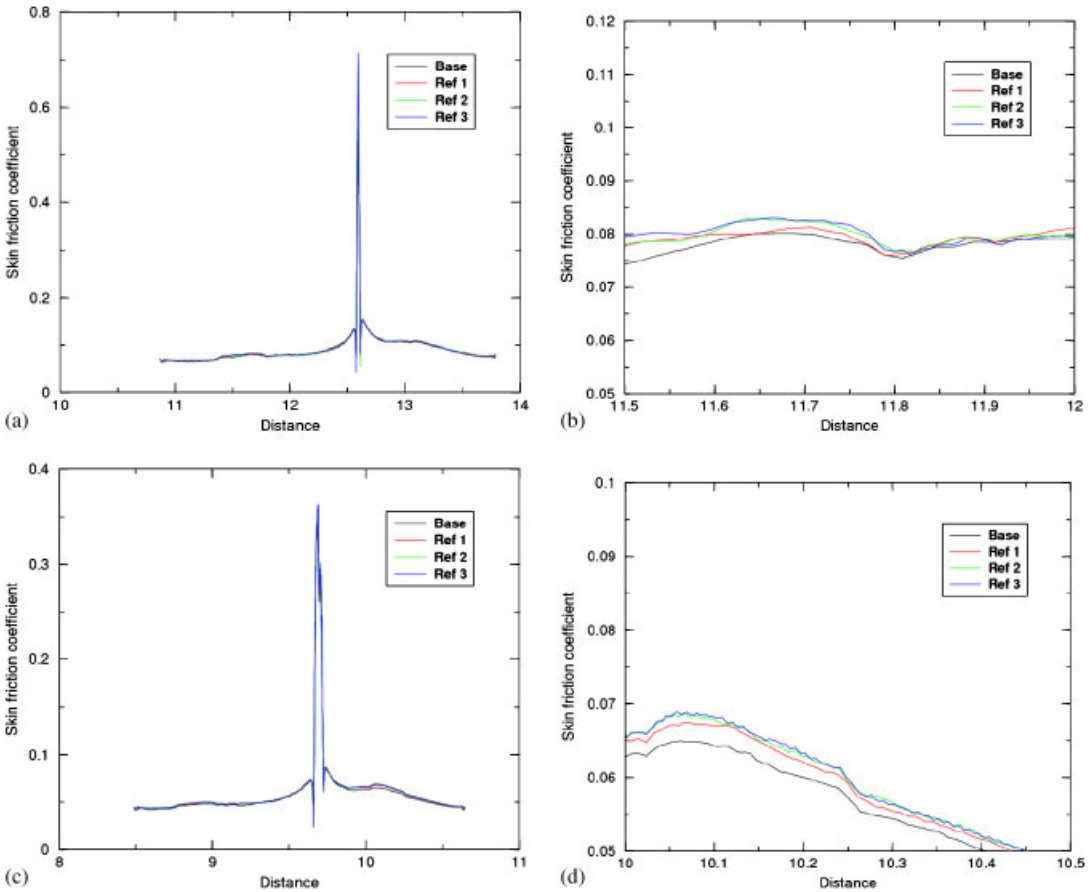

Figure 11. Distribution of skin friction coefficient c_f for the non-planar three-generation bronchial tube model: (a) segment 1; (b) segment 1 (detail); (c) segment 2; and (d) segment 2 (detail).

the computed skin friction distributions for refinements 2 and 3, but they are less than 1% of the average skin friction value for both the planar and non-planar three-generation models.

3.1.2. Mass flow distribution. The mass flow rates entering the branches for each of the four meshes for the planar and non-planar models were plotted to demonstrate mesh convergence of the primary flow. Figures 12 and 13 show the mass flow rate at locations aa', bb', cc', and dd' in the planar model (see Figure 8) for each refinement. Similarly, Figures 14 and 15 show the variation in mass flow with refinement in equivalent locations in the non-planar model. In these plots, refinement 0 corresponds to the baseline mesh. It should be noted that the y-axis scales vary significantly from plot to plot.

Convergence of the mass flow rate is observed in the planar and non-planar configurations in Figures 12 and 15. Slightly larger differences between refinements 2 and 3 were found at location dd' as shown in Figure 13(b) for the planar case and at location bb', as shown in Figure 14(b), for the non-planar case. However, the mass flow differences between refinements 2 and 3 were found to

DOI: 10.1002/fld

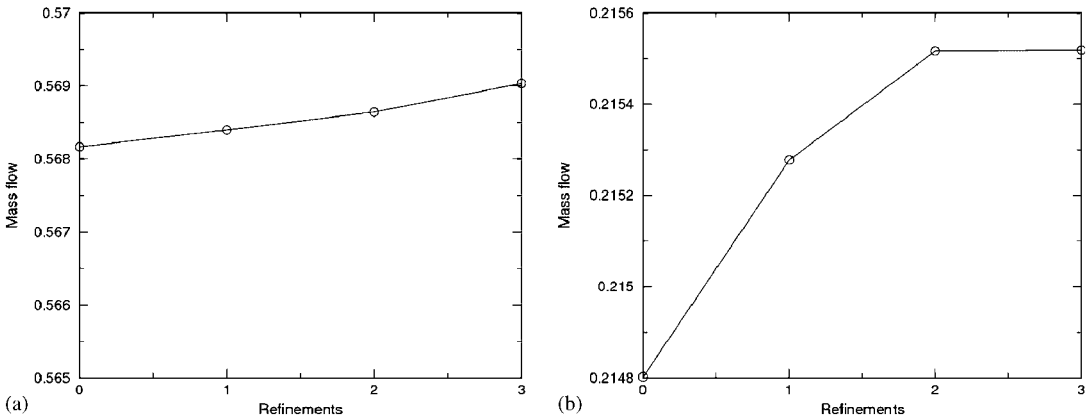

Figure 12. Variation of mass flow in second generation of planar model.
At locations (a) aa' and (b) bb'.

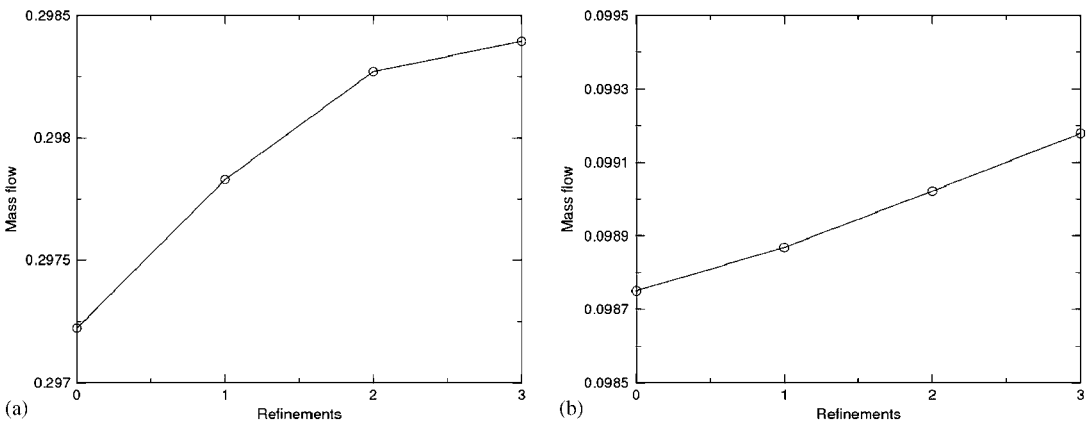

Figure 13. Variation of mass flow in third generation of planar model.
At locations (a) cc' and (b) dd'.

be less than 0.2% of the local average mass flow in each tube. This implies that mesh-independent solutions have been achieved for refinements 2 and 3 in terms of mass flow in each tube for both the planar and non-planar models.

3.1.3. Velocity profiles. Velocity profiles at different sections in the planar and non-planar airway models are shown in Figures 16–19. The velocity magnitude was extracted along a segment in the bifurcation plane for each of the cross-sections aa', bb', cc', and dd' (see Figure 8). The velocity was plotted as a function of distance along the segment. The distance was measured from the outside of the curve to the inside of the curve. It is evident from the velocity distribution plots that the differences become smaller as the mesh is refined. The differences between refinements

DOI: 10.1002/fld

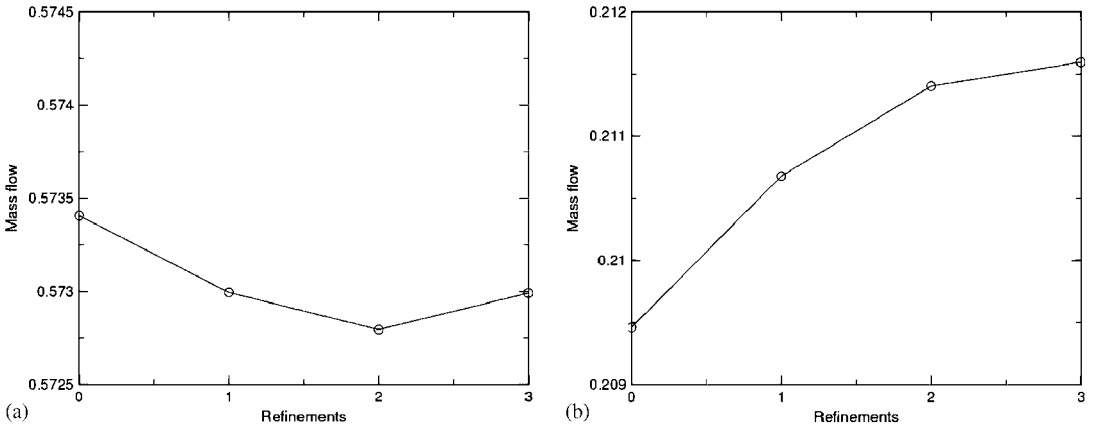

Figure 14. Variation of mass flow in second generation of non-planar model.
At locations (a) aa' and (b) bb'.

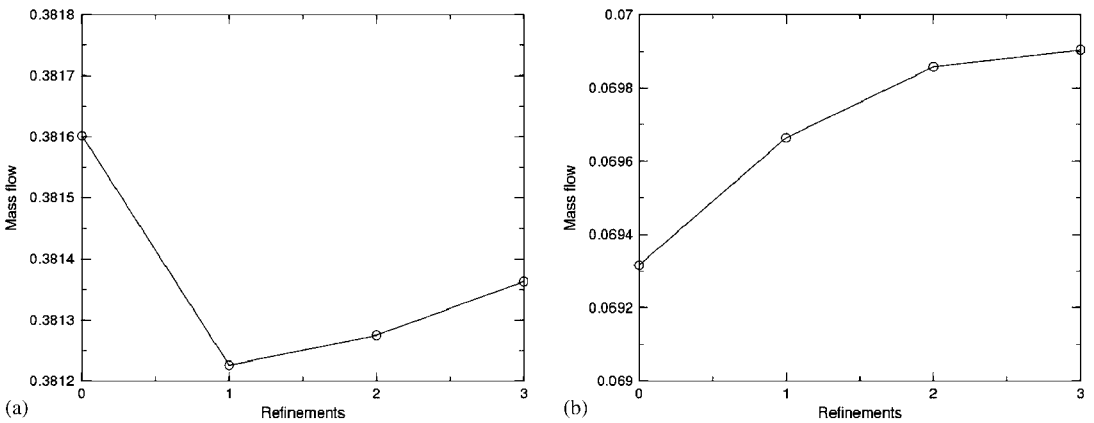

Figure 15. Variation of mass flow in third generation of non-planar model.
At locations (a) cc' and (b) dd'.

2 and 3 were found to be less than 1% of the local mean velocity. This suggests that the mesh-independent solution for primary flow has been achieved for refinement 2 mesh in both the planar and non-planar models.

Based on the skin friction coefficient distribution plots, mass flow distribution plots and velocity profiles, the primary flow on the meshes denoted as refinements 2 and 3 can be considered to be mesh independent for both the planar and non-planar configurations.

3.2. Effects of non-planarity on the primary flow

In this section, we compare primary flows computed for the planar and non-planar bronchial tube models. As the primary flow was shown to be mesh converged for refinement 2 in the previous

DOI: 10.1002/fld

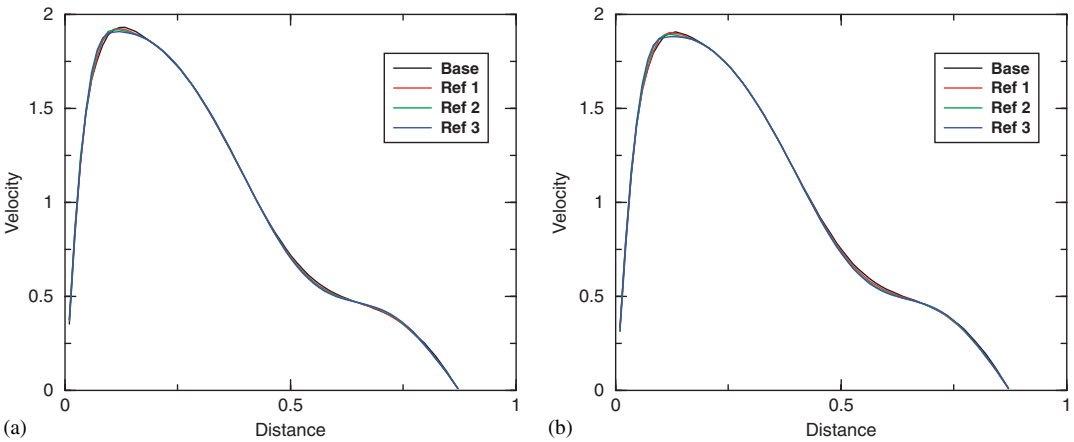

Figure 16. Velocity distribution in bifurcation plane at aa': (a) planar model and (b) non-planar model.

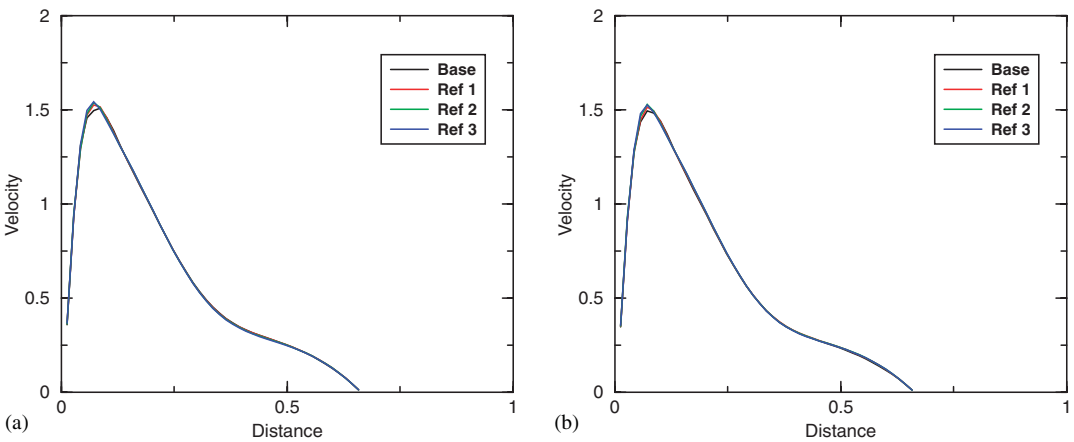

Figure 17. Velocity distribution in bifurcation plane at bb': (a) planar model and (b) non-planar model.

section, we utilize refinement 2 solutions for the planar and non-planar models in order to evaluate the combined effects of asymmetry and non-planarity on the primary flow.

3.2.1. Mass flow distribution. The mass flow fractions entering each tube for the planar and non-planar models are shown in Figure 20. The axial velocity profiles at various cross-sections for both the planar and non-planar models are also shown in Figure 20. In each case, the velocity profile is skewed toward the outside of the curve due to inertial effects. An unequal distribution of the flow is observed at the first bifurcation because of the asymmetry of the models. There is a slight difference in the flow distribution and flow profiles between the second-generation branching tubes of the planar and non-planar models. However, the differences are approximately 0.5% of the mass

DOI: 10.1002/fld

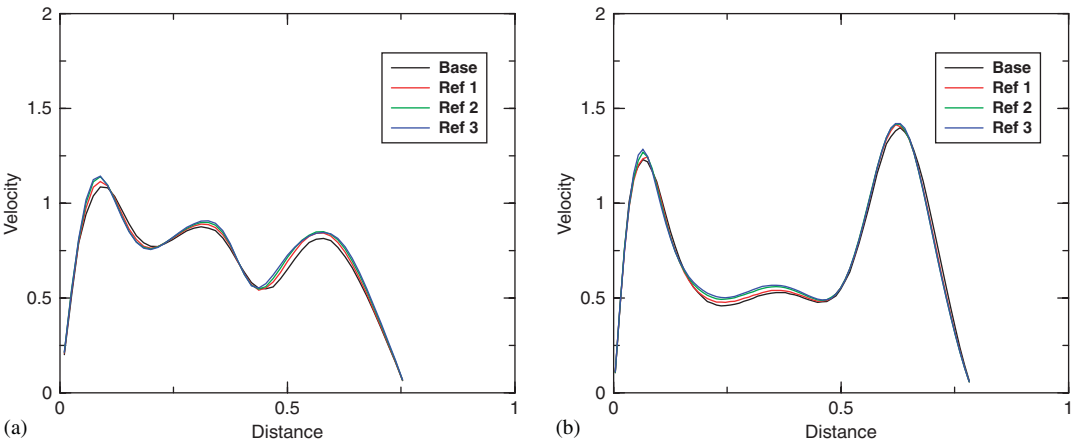

Figure 18. Velocity distribution in bifurcation plane at cc': (a) planar model and (b) non-planar model.

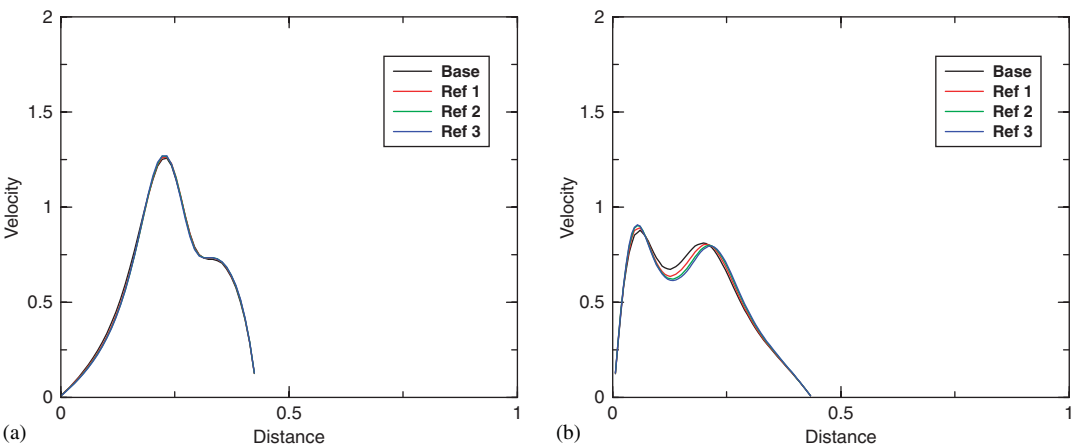

Figure 19. Velocity distribution in bifurcation plane at dd': (a) planar model and (b) non-planar model.

flow entering into the parent tube. This suggests minimal impact of non-planarity on the upstream flow.

In the planar case, where the second- and third-generation branching tubes are in the same plane and the velocity profiles are already skewed toward the medial branch, more flow will tend to go into the medial branching tubes. However, the medial branches are smaller in diameter than the lateral branches, resulting in almost equal flow partition in the third-generation tubes. In contrast, for the non-planar case, an imbalanced flow partition is observed because more flow goes into the larger tubes in the third-generation branches. These results can be contrasted to results from simulations of symmetric non-planar models that show a more balanced flow partitioning in the non-planar case than in the planar case [20] and demonstrate the importance of considering asymmetric branching in the geometric description.

DOI: 10.1002/fld

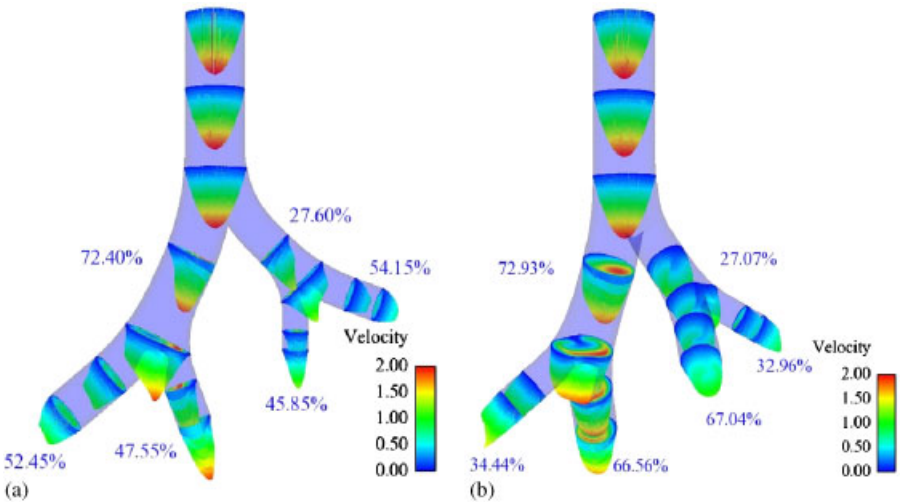

Figure 20. Mass flow fractions entering each tube of planar and non-planar models—axial velocity profiles colored by velocity magnitude: (a) planar model and (b) non-planar model (rotated for better view).

3.2.2. Velocity distribution. Velocity profiles for planar and non-planar cases are shown in Figures 21 and 22. We consider the sections passing through the center of the cross-section in the plane of the bifurcation as well as the plane normal to the bifurcation. The velocity profiles were plotted as a function of the distance from the edge of the tube. The distances are referenced relative to the diameter of the parent tube (unity).

The velocity profiles in the planar and non-planar cases are very similar as seen in Figures 21(a)–(d) and suggested by the mass flow partition discussed in the previous section. Again, this suggests that the non-planarity has little impact on the upstream flow. In the sections in the bifurcation plane, the velocity profiles are skewed toward the outside of the turn due to the effects of the turn as shown in Figures 21(a) and (c). In the plots where the sections are perpendicular to the bifurcation plane, the velocity profiles are deformed due to the presence of the secondary flows and generate the 'M-shaped' velocity profiles seen in Figures 21(b) and (d). This effect can also be seen clearly in Figure 9. These observations are in qualitative agreement with the experimental study by Schroter and Sudlow [7].

We now consider sections in the bifurcation plane in the third generation. Significant differences between the velocity profiles for the planar and non-planar models are observed at various sections as shown in Figures 22(a)–(d). This result illustrates the considerable impact of the non-planarity on the local velocity profiles. As observed previously, in the largest granddaughter tube (at cc'), higher velocities were found in the non-planar case (Figure 22(a)), whereas in the smallest granddaughter tube (at dd'), higher velocities were found in the planar case as shown in Figure 22(c). As the planar geometry is symmetric to the plane of bifurcation, this symmetry is evident in the velocity profiles for the planar model at the sections perpendicular to the bifurcation plane as shown in Figures 22(b) and (d). The same cannot be said about the non-planar model, as the symmetry with respect to the bifurcation plane is lost. The velocity profile in the normal section is not deformed (see Figure 22(d)) because the segment passes through the center of the tube and does not cross any of the vortices.

DOI: 10.1002/fld

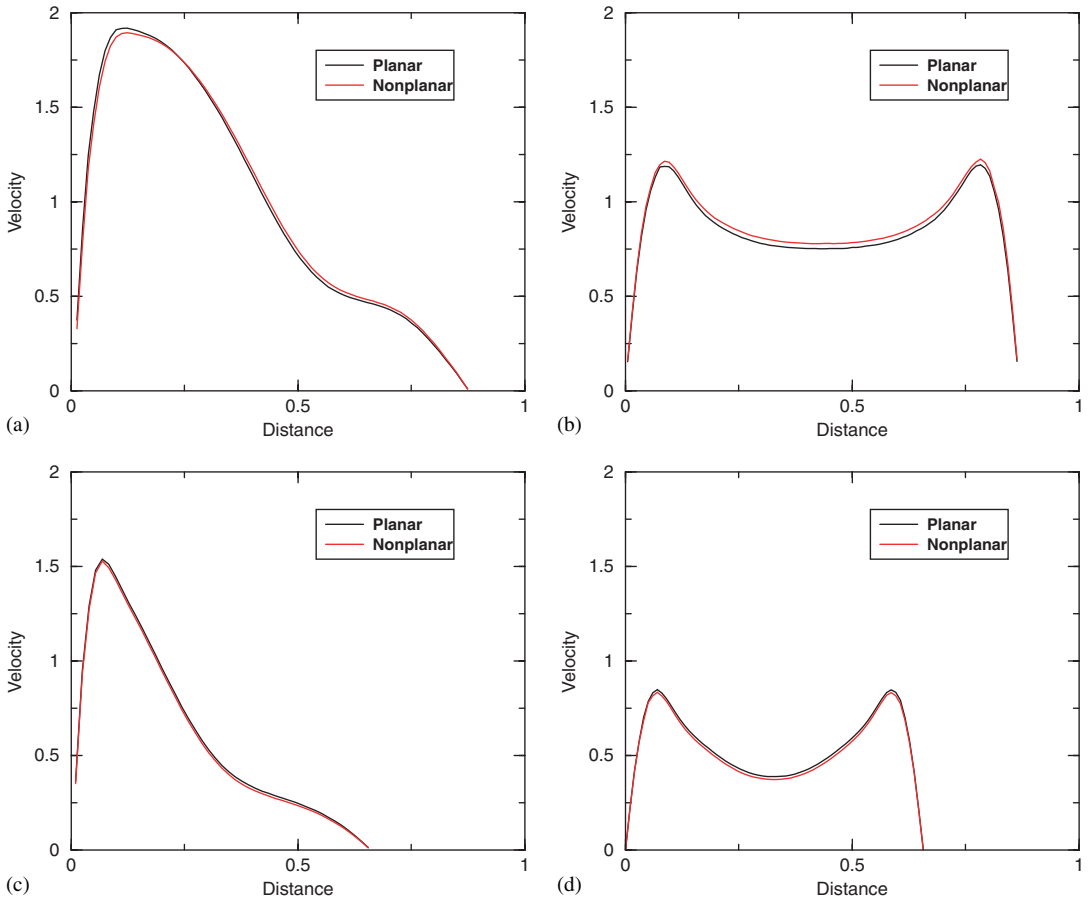

Figure 21. Comparison of the velocity distribution in second-generation branches of the planar and non-planar models: (a) in the bifurcation plane at aa'; (b) in the plane normal to the bifurcation at aa'; (c) in the bifurcation plane at bb'; and (d) in the plane normal to the bifurcation at bb'.

3.3. Mesh convergence of the secondary flow

The results from Section 3.1 only give an indirect indication of the mesh convergence of the secondary flows in a planar model. As we want to resolve secondary flow fields in the bronchial tube, we would like to measure the convergence of these vortex-dominated flows more directly. In this section, we analyze the effects of mesh refinement while concentrating on the secondary flow fields.

The location of a vortex core is one of the important physical attributes of a vortex. Therefore, we have chosen the difference in vortex core position between refinements as a metric to assess mesh independence of the secondary flow. The vortex core position was estimated using the automated vortex characterization software described by Jankun-Kelly *et al.* [28]. This software provides a sub-cell estimate of the vortex core position. The vortex corelines were extracted for the planar and non-planar three-generation bronchial tube models and are shown in Figures 23(a) and (b),

DOI: 10.1002/fld

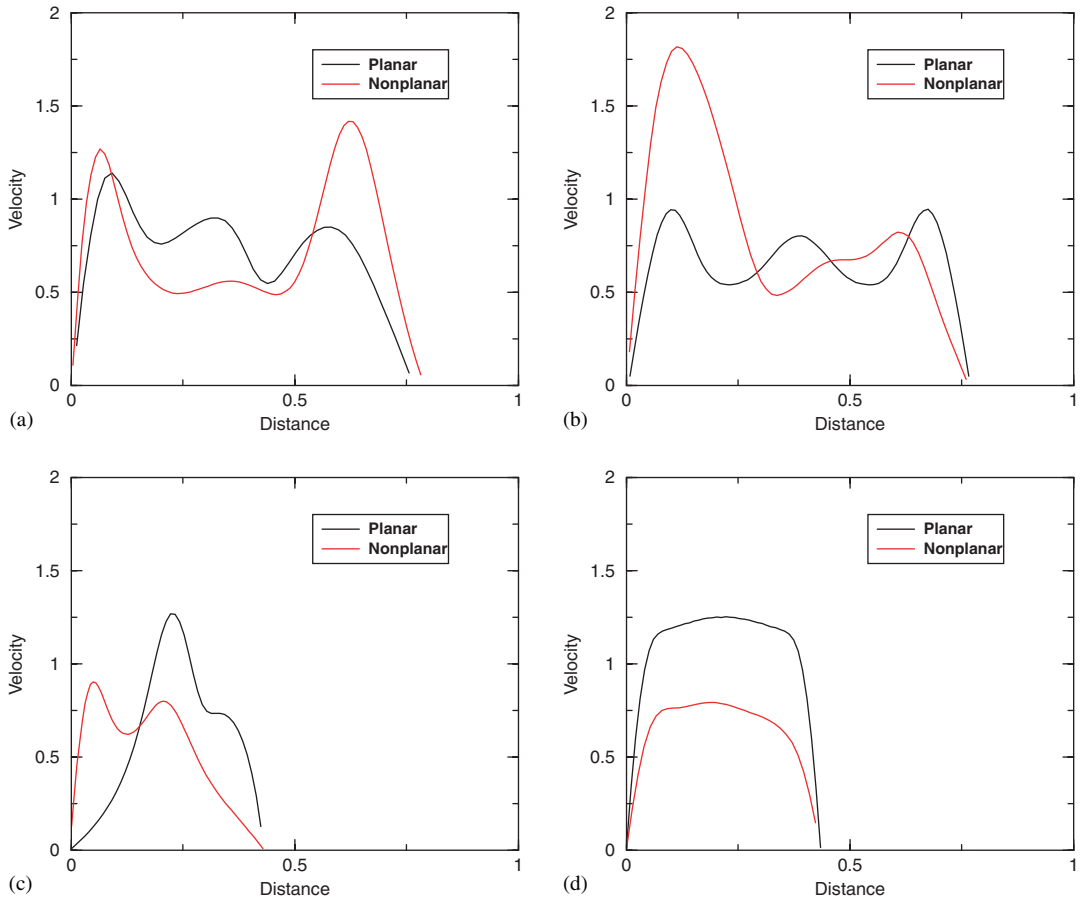

Figure 22. Comparison of the velocity distribution in third-generation branches of the planar and non-planar models: (a) in the bifurcation plane at cc'; (b) in the plane normal to the bifurcation at cc'; (c) in the bifurcation plane at dd'; and (d) in the plane normal to the bifurcation at dd'.

respectively. The corelines are colored by the direction of rotation of the vortices. Here, green-colored vortices are rotating in the clockwise direction with respect to the primary flow whereas purple-colored vortices are rotating in the counter-clockwise direction.

To view the vortex patterns in each cross-section, the cross-flow velocity vectors were plotted on the cutting plane, which was shaded by total velocity magnitude. Only every third vector was plotted for clarity. In these images, we have explicitly indicated the orientations of the bifurcation plane (BB') and the plane normal to the bifurcation plane (NN'). We first consider the counter-rotating vortex pair in the daughter tubes after the first bifurcation as seen in Figures 24(a) and (b) at cross-sections aa' and bb' in Figure 8, respectively. Figures 25(a) and (b) show the core locations as a function of the number of mesh refinements for the planar and non-planar models. The baseline mesh is again designated as refinement 0 in the plots. The vortex location is expressed in terms of the distance from the center of the cross-section to the estimated vortex core position. The error

DOI: 10.1002/fld

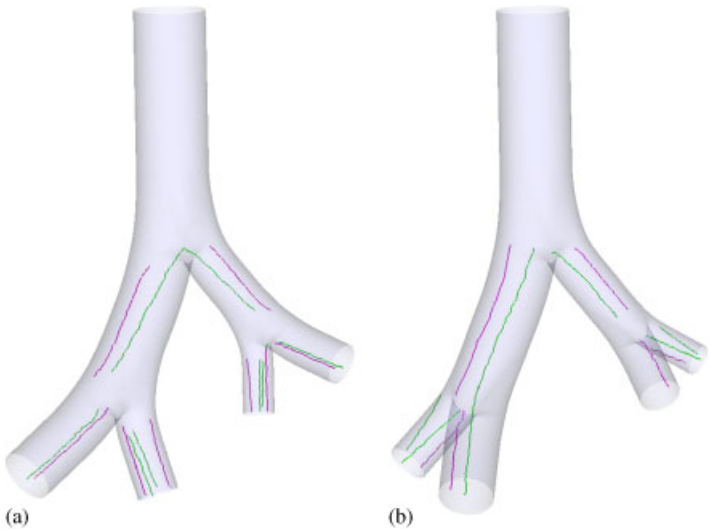

Figure 23. Vortex corelines colored by their rotation with respect to the axial velocity (green—clockwise and purple—counter-clockwise): (a) planar model and (b) non-planar model.

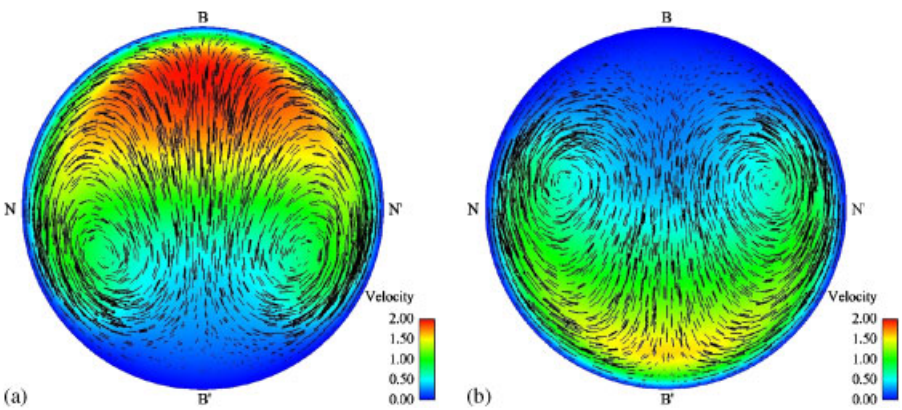

Figure 24. Vortex pair in second generation (cross-flow velocity vectors on a cutting plane colored by velocity magnitude): vortices in cross-sections (a) aa' and (b) bb'.

bars in each plot represent the diagonal of an element in a local uniform grid employed by the vortex detection software to estimate the position of the vortex core inside of the cell and provide a measure of the uncertainty in the estimated vortex position.

As can be seen in Figures 25(a), 26(a) and (b) there are only nominal differences between the left and right vortex core locations for the solutions computed after two refinements and three refinements. Further, these differences are within the corresponding error bounds. This is not the case in the larger daughter tube of the non-planar model as shown in Figure 25(b). However, the

DOI: 10.1002/fld

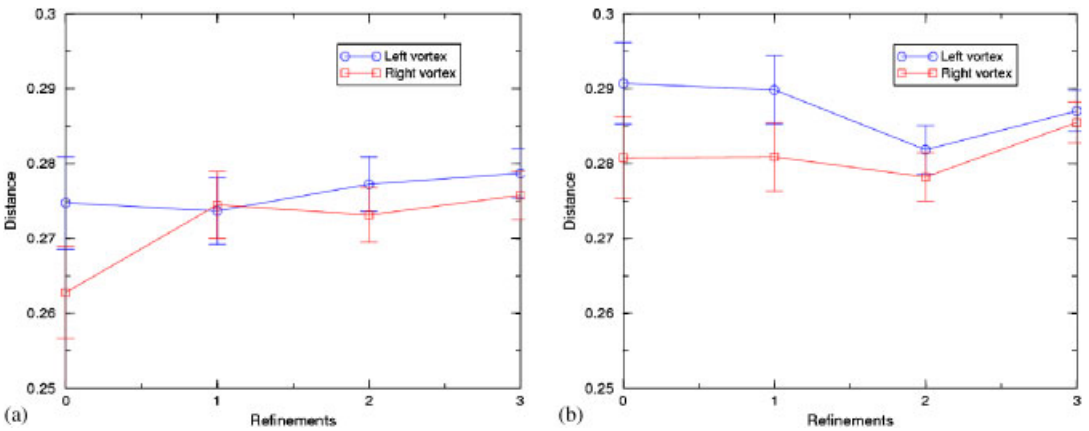

Figure 25. Variation of vortex positions in cross-section aa' (local edge length = 0.015): (a) planar model and (b) non-planar model.

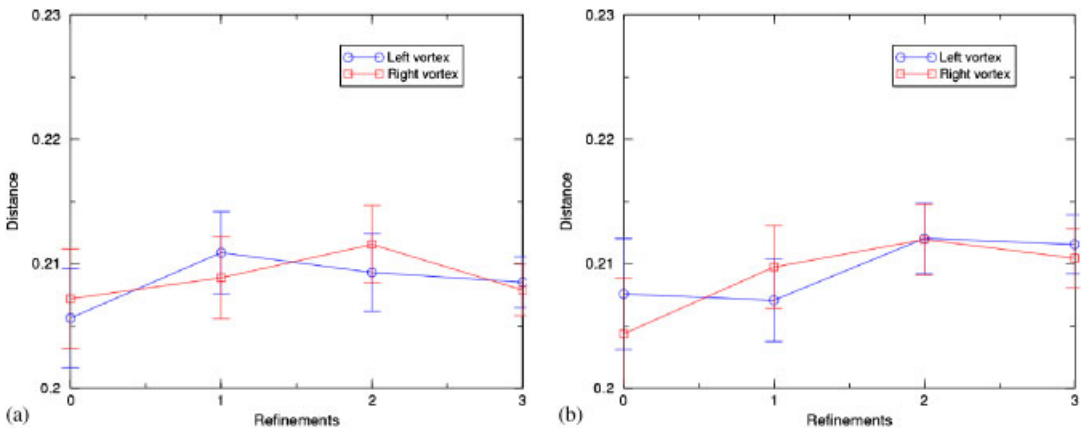

Figure 26. Variation of vortex positions in cross-section bb' (local edge length = 0.011): (a) planar model and (b) non-planar model.

changes in the vortex core positions are less than the local edge length in the mesh for refinement 3 (0.015), again suggesting that we are approaching a mesh-independent solution for both the planar and non-planar cases. It should be noted that, within each cross-section, the left and right vortices are located at nearly the same position. This is because both the planar and non-planar models are symmetric in the second generation with respect to the bifurcation plane.

We now consider cross-sections in the third generation for the planar and non-planar cases at section cc' (see Figure 8). The symmetric vortex pattern for the planar model is seen in Figure 27(a), whereas the asymmetric vortex pattern is seen in Figure 28 for the non-planar model. The plots of vortex positions as a function of refinement are shown in Figure 27(b) for the planar case. Because the vortices here are symmetric, the distances for both the left and right vortex cores are nearly

DOI: 10.1002/fld

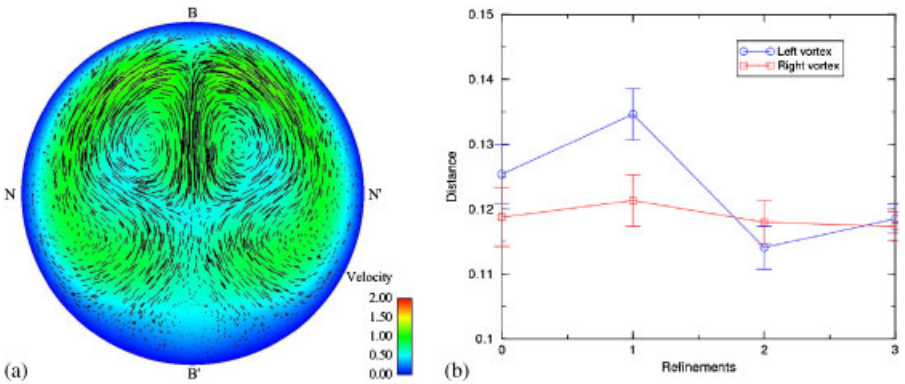

Figure 27. Mesh convergence of secondary flows in cross-section cc'—planar model: (a) vortices in cross-section cc' (cross-flow velocity vectors on a cutting plane colored by velocity magnitude) and (b) variation of vortex positions (local edge length = 0.01).

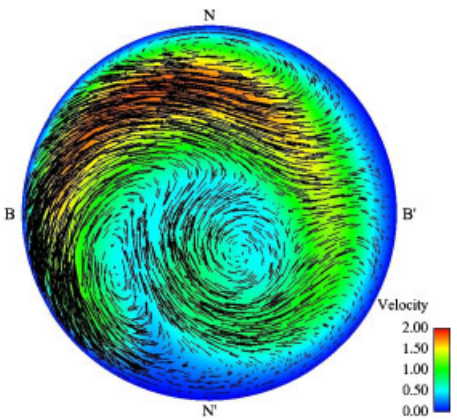

Figure 28. Vortices in cross-section cc' (cross-flow velocity vectors on a cutting plane colored by velocity magnitude)—non-planar model.

the same. As the vortex core distance in the non-planar case varies considerably for the left and right vortices, the vortex positions were plotted in separate figures. Figures 29(a) and (b) show the variation of the vortex core locations as a function of the refinement. For both the planar and non-planar models, the plots show convergence of the vortex core positions at refinement 2 based on the local edge lengths at cross-section cc'.

The vortex patterns and vortex position plots in the smallest granddaughter tube for the planar and non-planar models are shown in Figures 30–32. Two symmetric vortex pairs are observed in Figure 30 for the planar model. The asymmetry in the non-planar vortex pattern is again evident from Figure 32(a). Convergence of the estimated vortex core positions with mesh refinement for the planar and non-planar models is demonstrated in Figures 31(a) and (b) and 32(b). The symmetry of the vortices in the planar model is evident from the vortex position plots. Figures 31(a) and (b)

DOI: 10.1002/fld

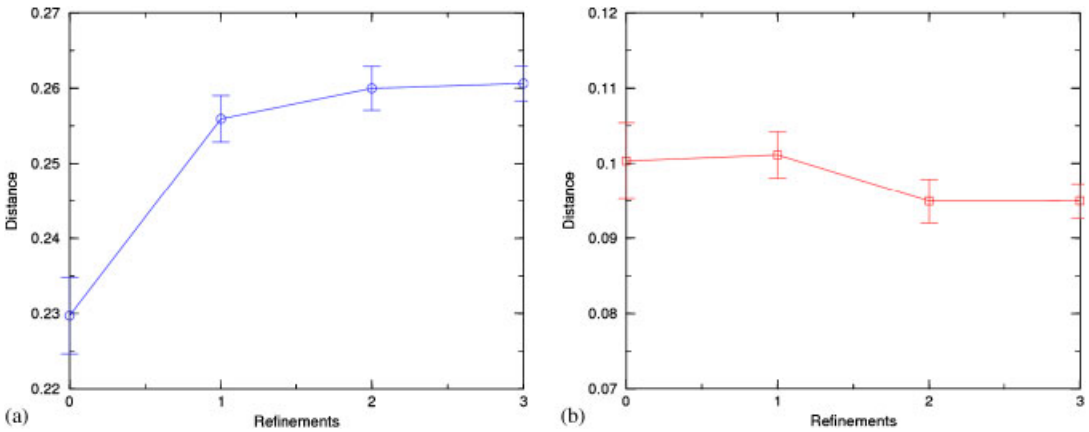

Figure 29. Mesh convergence of secondary flows in cross-section cc' (local edge length = 0.01)—non-planar model: variation of (a) left vortex position and (b) right vortex position.

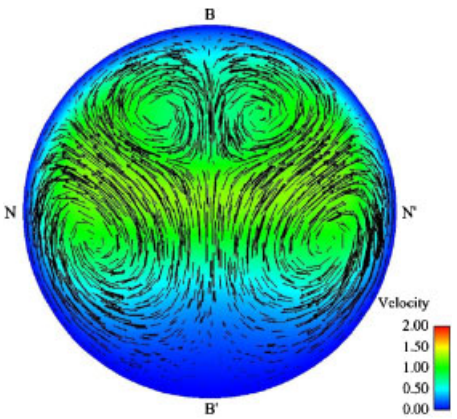

Figure 30. Vortices in cross-section dd' (cross-flow velocity vectors on a cutting plane colored by velocity magnitude)—planar model.

illustrate that changes in the vortex core positions between refinements 2 and 3 are within the local cell size (0.007). Hence, it can be concluded that the vortex core positions are converged for refinement 2 in cross-section dd' for the planar model. The same can be concluded from Figure 32(b) for the vortices in the cross-section dd' for the non-planar model. This indicates that the secondary flows have become mesh independent for refinement 2 in the smallest granddaughter tube for both the planar and non-planar models.

3.4. Effects of non-planarity on the secondary flows

In this section we compare the results from simulation of the secondary flows in the planar and non-planar asymmetric bronchial tube models. As the secondary flows were shown to be converged

DOI: 10.1002/fld

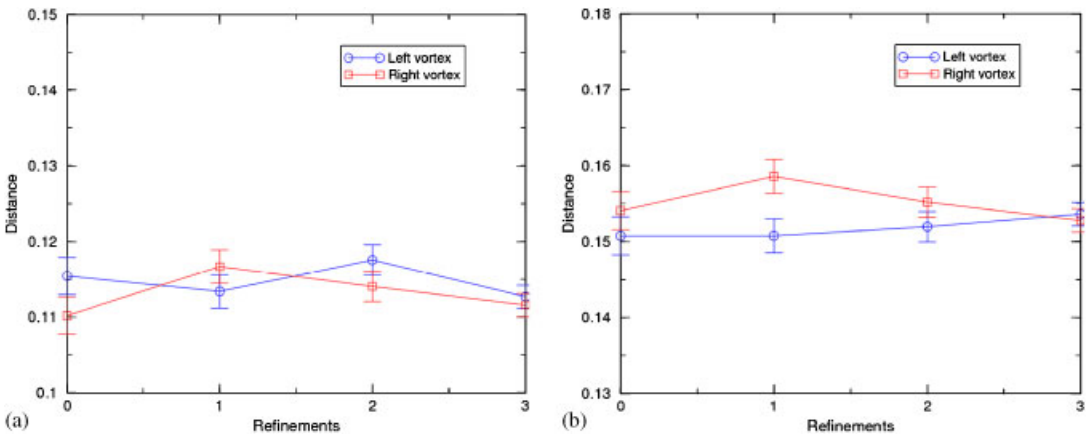

Figure 31. Mesh convergence of secondary flows in cross-section dd' (local edge length = 0.007)—planar model: variation of (a) top vortex pair positions and (b) bottom vortex pair positions.

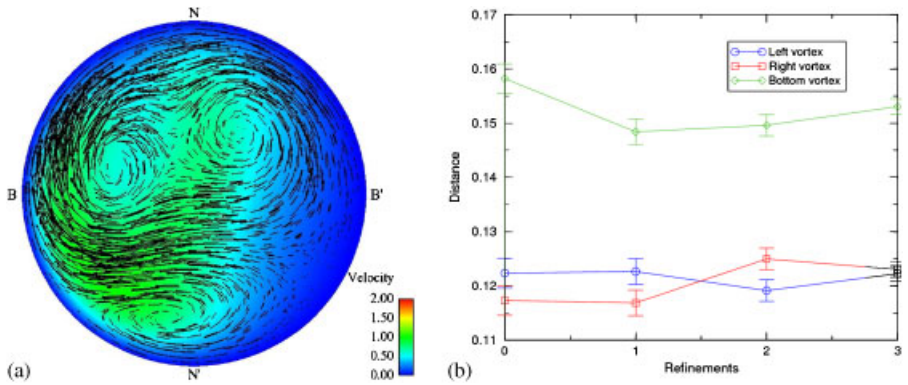

Figure 32. Mesh convergence of secondary flows in the cross-section dd'—non-planar model: (a) vortices in cross-section dd' (cross-flow velocity vectors on a cutting plane colored by velocity magnitude) and (b) variation of vortex position (local edge length = 0.007).

for refinement 2 in the previous section, we use refinement 2 solutions of the planar and non-planar models in order to evaluate the effects of non-planarity on the secondary flows.

The vortex corelines in the planar and non-planar models are shown in Figure 23. We consider the planar case first. After the first bifurcation, a vortex pair is generated in both the larger and the smaller daughter tubes. The velocity profile entering the medial branch of the larger daughter branch is skewed toward the inside of the turn, resulting in a low-momentum region at the wall on the outside of the turn as shown in Figure 20(a). A vortex pair is generated due to this low momentum at the wall outside of the turn. Also, a vortex pair is generated at the inside wall of the turn. The four resulting vortices are seen in the medial branch in Figure 30. The same is not true for the lateral branches due to the low-momentum region at the inside of the turn; only a single vortex pair is generated in the lateral branches as seen in Figure 27(a).

DOI: 10.1002/fld

We now consider the vortices in the non-planar airway model. As seen in Figure 23(b), the vortices generated after the first bifurcation have a significant effect on the vortices generated after the second bifurcation. Let us focus on the third-generation branching off the larger daughter tube first. It is clearly seen from the figure that the vortex from the larger daughter tube continues into the third-generation larger tube. The newly generated vortex pair is overpowered by the previously existing vortices and only a single vortex pair exists in the largest granddaughter tube as shown in Figure 28. In the smaller granddaughter off the smaller daughter tube, three distinct vortices are seen in Figure 32(a). A vortex pair is generated here due to the turning of the flow. The secondary flows in the asymmetric non-planar model are quite complex in comparison with the secondary flows in the symmetric non-planar models described in the literature [18, 20]. In the symmetric non-planar three-generation case, the vortices in the second-generation daughter tubes split and each goes into a separate daughter tube in the third generation.

4. CONCLUSIONS

An in-depth study of steady-state laminar inspiratory flows in planar and non-planar, three-generation asymmetric airway models was performed. Comparisons of the primary and secondary flows for the planar and non-planar geometries were made in order to understand the combined effects of asymmetry and non-planarity. A mesh refinement study was performed to assure that the solutions were mesh independent. The following conclusions can be drawn from the numerical results:

1. The vortical flow patterns in the third-generation branches were significantly different in the planar and non-planar configurations. As the planar model is symmetric with respect to the bifurcation plane, the vortices produced symmetric patterns. This symmetry was lost in the non-planar model and asymmetric vortex patterns were observed. The secondary flows become quite complex when both non-planarity and asymmetry are included in the bronchial tube models.
2. The mass flow distribution in the third-generation branches were the most affected by non-planarity. An imbalanced flow distribution was observed in the non-planar case in contrast to the planar case. The velocity profiles at equivalent sections were quite different in the planar and non-planar cases. The effect of non-planarity was shown to be minimal on the upstream primary flows.
3. Mesh-independent solutions were obtained for primary as well as secondary flows after the second refinement in planar and non-planar three-generation airway models. The vortex position was used as a metric to demonstrate mesh independence for the secondary flows. The vortex core locations in the third-generation branches were not found to be within the sub-cell error bound. However, the vortex positions were within the local edge lengths in refinements 2 and 3 demonstrating mesh independence of the solution on these meshes.

ACKNOWLEDGEMENTS

The support of the National Science Foundation (EPS-0556308 and ITR/NGS-0326386) is gratefully acknowledged. The authors thank the reviewers for their careful reviews and many helpful suggestions. We also thank Monika Jankun-Kelly for her assistance with the vortex detection software.

DOI: 10.1002/fld

REFERENCES

1. Gatlin B, Cuichhi C, Hammersley J, Olson D, Reddy R, Burnside G. Computation of converging and diverging flow through an asymmetric tubular bifurcation. *The 1997 ASME Fluids Engineering Division Summer Meeting*, *ASME FEDSM97-3429*, Vancouver, BC, Canada, 1997; 1–7.
2. Dean W. The stream-line motion of fluid in a curved pipe. *Philosophical Magazine* 1928; **30**:673–695.
3. Weibel ER. *Morphometry of the Human Lung*. Academic Press: New York, 1963.
4. Horsfield K, Cumming G. Morphology of the bronchial tree in man. *Journal of Applied Physiology* 1968; **24**:373–383.
5. Hammersley J, Olson D. Physical models of the smaller pulmonary airways. *Journal of Applied Physiology* 1992; **72**:2402–2414.
6. Hegedus J, Balashazy I, Farkas A. Detailed mathematical description of the geometry of airway bifurcations. *Respiratory Physiology and Neurobiology* 2004; **141**:99–114.
7. Schroter R, Sudlow M. Flow patterns in models of the human bronchial airways. *Respiration Physiology* 1969; **7**:341–355.
8. Balashazy I, Hofmann W. Particle deposition in airway bifurcation—I. Inspiratory flow. *Journal of Aerosol Science* 1993; **24**(6):745–772.
9. Balashazy I, Hofmann W. Particle deposition in airway bifurcation—II. Expiratory flow. *Journal of Aerosol Science* 1993; **24**(6):773–786.
10. Liu Y, So R, Zhang C. Modeling the bifurcating flow in an asymmetric human lung airway. *Journal of Biomechanics* 2003; **36**:951–959.
11. Soni B, Thompson D. Secondary flows in the small bronchial tubes: a mesh refinement study. *AIAA Paper 2006-3518 Presented at the AIAA 36th Fluid Dynamics Conference*, San Francisco, CA, 2006.
12. Zhang Z, Kleinstreuer C, Kim C. Flow structure and particle transport in a triple bifurcation airway model. *Transactions of ASME* 2001; **123**:320–330.
13. Zhang Z, Kleinstreuer C, Donohue J, Kim C. Comparison of micro- and nano-size particle depositions in a human upper airway. *Aerosol Science* 2005; **36**:211–233.
14. Balashazy I, Moustafa M, Hofmann W, Szoke R, El-Hussein A, Ahmed A. Simulation of fiber deposition in bronchial airways. *Inhalation Toxicology* 2005; **17**:717–727.
15. Longest P, Vinchurkar S. Effects of mesh style and grid convergence on particle deposition in bifurcating airway models with comparisons to experimental data. *Medical Engineering and Physics* 2007; **29**:350–366.
16. Sera T, Fujioka H, Yokota H, Makinouchi A, Himeno R, Schroter R, Tanishita K. Three-dimensional visualization and morphometry of small airways from microfocal X-ray computed tomography. *Journal of Biomechanics* 2003; **36**:1587–1594.
17. Kim C, Fisher D. Deposition characteristics of aerosol particles in sequentially bifurcating airway models. *Aerosol Science and Technology* 1999; **31**:198–220.
18. Caro CG, Schroter R, Watkins N, Sherwin SJ, Sauret V. Steady inspiratory flow in planar and non-planar models of human bronchial airways. *Proceedings of the Royal Society of London*, *Series A* 2002; **458**: 791–809.
19. Comer J, Kleinstreuer C, Kim S. Flow structures and particle deposition patterns in double-bifurcation airway models. Part 2: aerosol transport and deposition. *Journal of Fluid Mechanics* 2001; **435**:55–80.
20. Liu Y, So R, Zhang C. Modeling the bifurcating flow in a human lung airway. *Journal of Biomechanics* 2002; **35**:465–473.
21. Zhang Z, Kleinstreuer C. Transient airflow structures and particle transport in a sequentially branching lung airway model. *Physics of Fluids* 2002; **14**(2):862–880.
22. Nowak N, Kadake P, Annapragada A. Computational fluid dynamics simulation of airflow and aerosol deposit ion in human lungs. *Annals of Biomedical Engineering* 2003; **31**:374–390.
23. Ertbruggen C, Hirsch C, Paiva M. Anatomically based three-dimensional model of airways to simulate flow and particle transport using computational fluid dynamics. *Journal of Applied Physiology* 2004; **98**: 970–980.
24. Gaither J, Marcum D, Mitchell B. Solid mesh: a solid modeling approach to unstructured grid generation. *Seventh International Conference on Numerical Grid Generation in Computational Field Simulations*, Whistler, BC, 2000; 829–838.
25. Marcum D, Weatherill N. Unstructured grid generation using iterative point insertion and local reconnection. *AIAA Journal* 1995; **33**:1619–1625.

DOI: 10.1002/fld

26. Hyams D. An investigation of parallel implicit solution algorithms for the incompressible Navier–Stokes equations. *Ph.D. Thesis*, Mississippi State University, 2000.
27. Chorin AJ. A numerical method for solving incompressible viscous flow problems. *Journal of Computational Physics* 1967; **2**:12–26.
28. Jankun-Kelly M, Jiang M, Thompson D, Machiraju R. Vortex visualization for practical engineering applications. *IEEE Transactions on Visualization and Computer Graphics* 2006; **12**(6):957–964.

DOI: 10.1002/fld